JOURNAL OF AIRCRAFT
Vol. 47, No. 6, November–December 2010

Particle Swarm Optimization of Suction and Blowing on Airfoils at Transonic Speeds

Y. Volkan Pehlivanoglu*
Turkish Air Force Academy, 34149 Istanbul, Turkey
and
Bedri Yagiz,† O. Kandil,‡ and O. Baysal§
Old Dominion University, Norfolk, Virginia 23529

DOI: 10.2514/1.C000233

To improve the aerodynamic performance, the control applied to the transonic flow past an airfoil is optimized. The flow is simulated by solving the Navier–Stokes equations and a turbulence model. The control is applied using flow suction or blowing on the airfoil surface. The design variables are set to be the location and the angle of the suction/blowing port and the mass flow coefficient at this port. To validate the computational methodology, successful comparisons have been made with available experimental data. The focus of the present study is on the application of a selected design optimization methodology. Therefore, the particle swarm optimization algorithm is also validated by comparing its results with those from a more traditional approach: that is, a gradient-based method with sequential quadratic programming. It is observed that the aerodynamic performance is increased by over 20% as a result of optimizing the location, angle, and mass flow coefficient of the suction and blowing control ports on the airfoil surface at transonic speeds.

Nomenclature

C_D	=	drag coefficient
C_L	=	lift coefficient
C_p	=	pressure coefficient
C_q	=	mass flow coefficient
c	=	chord of the airfoil
L/D	=	lift-to-drag ratio
x_c	=	center location of actuator
α	=	angle of attack
β	=	actuator jet angle

I. Introduction

ENGINEERING design of an airplane wing roughly consists of three stages: conceptual design, such as determining the span length, maximum thickness, taper ratio, sweep angle, and aspect ratio; preliminary design, including airfoil shape and its optimization; and detailed design, including the detailed plan for manufacturing of the wing. In a preliminary design phase, designers start with a good baseline design and then concentrate on improving its performance by using some optimization techniques. For transonic commercial aircraft wing design, the primary goal is to improve the wing performance at the cruise conditions without severe penalty at offdesign conditions. The main issue at this stage is a shock-wave-reduction problem. A wave drag is caused by the formation of shock waves around the wing. Shock waves radiate away a considerable amount of energy that is experienced by the aircraft as drag. The magnitude of the rise in drag is impressive, typically peaking at about four times the normal subsonic drag. As this consumes energy, it is highly beneficial to eliminate the effects of shock wave at the design phase. It may be worth recalling that a mere 10% reduction in the total drag of an aircraft translates into a saving of billions in annual fuel cost for the commercial aircraft in the world [1]. Optimization is a key tool to reduce the effects of shock wave and it is heavily based on the reforming of an airfoil shape in a passive way. Although passive control enhances the aerodynamic performance at the design point, it may have harmful effects at offdesign conditions. Furthermore, it may not be practically applicable for the current designs in service. An active flow control may be an alternative remedy. In this context, active flow control may offer new solutions for the performance maximization of existing designs [2].

Active flow control (AFC) has been a topic of major research in fluid mechanics for more than two decades. There are numerous published studies to enable active flow control benefits on airfoils at subsonic speeds [3–5]. However, there are few studies related to shock wave reduction based on active flow control at transonic flows. The small disturbance close to the shock can result in large changes in the performance of the airfoil at transonic and supersonic speeds [6]. The experimental study of Smith and Walker [7] has shown that applying strong suction in the strong adverse pressure gradient increases the lift. Qin et al. [8] showed that lift could be increased by applying suction in the vicinity of the shock; however, this is obtained with an increase in drag. Injection of momentum accelerates the inviscid outer flow over the airfoil ahead of the shock, which induces weak compression waves that soften the adverse pressure gradient [9]. In these aforementioned studies, only one actuator was used for suction or blowing. As a result of this study, it was seen that one actuator is not enough to obtain the desired goal. Vadillo and Agarwal [10] have investigated the same problem as others and concluded that three synthetic jet actuators were needed on the upper surface of the airfoil to enhance the L/D ratio with minimum change in transonic drag. Although AFC provides such degrees of improvements, the sensibility of aerodynamic performance to active flow control design parameters makes it a nontrivial and expensive problem [11]. Therefore, the designer has to optimize a number of different parameters related to active flow control. Yagiz and Kandil [12] evaluated the capability of weakening the shock waves to improve the aerodynamic performance in transonic conditions by using surface suction/blowing on airfoils via gradient-based optimization process. They selected the suction/blowing speed and angle as

Presented as Paper 2009-3763 at the 27th AIAA Applied Aerodynamics Conference, San Antonio, TX, 22–25 June 2009; received 21 December 2009; revision received 11 August 2010; accepted for publication 20 August 2010.

*Major, Turkish Air Force; vpehlivan@hho.edu.tr.
†Graduate Research Assistant, Aerospace Engineering Department. Student Member AIAA.
‡Professor and Eminent Scholar, Aerospace Engineering Department. Associate Fellow AIAA.
§Dean, Professor and Eminent Scholar, Batten College of Engineering and Technology. Associate Fellow AIAA.

design parameters for different numbers of control points keeping the locations fixed. However, the missing parameter, the location of an actuator, is also an important design variable for this problem.

The desired goal of the present study is to improve the aerodynamic performance on airfoils at transonic speeds by optimizing the surface suction/blowing parameters. For this application, a non-gradient-based global algorithm, particle swarm optimization, method is used to search for an improved design. For selected cases, obtained results are compared to those from a gradient-based algorithm. For the flow simulations, a time-dependent, turbulent flow solver developed at NASA Langley Research Center is used on structured grids. Present computations were performed for Mach 0.78 flow past a NACA 64A010 airfoil at an angle of attack of 0.5° with and without AFC. The experimental data by Smith and Walker [7] for the same conditions was used to validate the present computational study. From the obtained results it was observed that the aerodynamic performance is increased by over 20% as a result of optimizing the location, angle, and mass flow coefficient of the suction and blowing control ports on the airfoil surface.

II. Mathematical Model

A. Numerical Model for Flow Analysis

A widely used computational fluid dynamics (CFD) code [13] was used to perform the computational simulations. The thin-layer approximation to the time-dependent conservation form of the Reynolds-averaged Navier–Stokes equations is solved by an implicit, approximately factored, finite volume, upwind, and multigrid algorithm. Because of the high Reynolds number of the flow, it was assumed to be fully turbulent. Spalart–Allmaras (SA) models appear to be more susceptible to shock effects [14]. Therefore, a one-equation SA model was used to compute the turbulent eddy viscosity. Although the other available turbulence models were also tested on the validation case, the best agreement between the model predictions and the experimental data was provided by the SA model. The details of the code can be found in Krist et al. [13]. A two-level multigrid technique was used to achieve the convergence acceleration. The calculation is initiated from a steady-state solution obtained for the flow in the absence of any jets. Then the control cases are started from this steady solution until the residual is driven down to 10^{-9}. The actuator is modeled as a boundary condition that computes the mass flow through a solid boundary. The mass flow coefficient is defined as the ratio between the boundary and the freestream mass flows:

$$C_q = \frac{(\rho u)}{(\rho u)_\infty}, \qquad C_q = \int_0^{T_{\text{st}}} C_{qu}\, \mathrm{d}t\dagger \tag{1}$$

First, a constant rate of change in the mass flow, C_{qu}, is established. Then C_q is gradually increased from zero to a constant value within T_{st} (time for stable initiation) and then it is kept fixed [13].

B. Optimization

1. Particle Swarm Optimization Algorithm

As in other evolutionary algorithms, the particle swarm optimization (PSO) method is a population-based stochastic algorithm that originates from the nature and evolutionary computations. These algorithms may often require more cost-function evaluations than comparable gradient-based algorithms. However, they provide attractive characteristics, such as ease of implementation for both continuous and discrete problems, efficient use of large numbers of parallel processors, no requirement for the continuity in response functions, and more robust solution generations for searching global or near-global solutions. PSO algorithms search the optimum within a population called swarm. It benefits from two types of learning, such as cognitive learning based on an individual's own history and social learning based on a swarm's own history, accumulated by sharing information among all particles in the swarm. Since its development in 1995 by Eberhart and Kennedy [15], it has attracted significant attention and popularity.

A general optimization problem can be expressed as follows:

$$\begin{aligned} &\min f(\boldsymbol{x}) \\ &\text{Subject to } g_j(\boldsymbol{x}) \le 0 \quad j = 1, 2, \ldots, m \\ &h_k(\boldsymbol{x}) = 0 \quad k = 1, 2, \ldots, l \\ &\boldsymbol{x}^L \le \boldsymbol{x} \le \boldsymbol{x}^U \end{aligned} \tag{2}$$

where $\boldsymbol{x}$ is a column vector of real-valued design variables, $f(\boldsymbol{x})$ is the objective function, g_j is the set of inequality constraints, h_k is the set of equality constraints, and $\boldsymbol{x}^L$ and $\boldsymbol{x}^U$ are the side constraints for the design variables. For the present PSO setup, let S be the swarm size, let D be the particle dimension space, and each particle of the swarm has a current position vector $\boldsymbol{x}_i$, current velocity vector $\boldsymbol{v}_i$, and individual best-position vector $\boldsymbol{P}_i$ found by the particle itself. The swarm also has the global best-position vector $\boldsymbol{P}_g$ found by any particle during all prior iterations in the search space. Assuming that the function f is to be minimized, and describing the following notations in tth generation, then the definitions are as follows:

$$\begin{aligned} &\boldsymbol{x}_i(t) = (x_{i,1}(t), x_{i,2}(t), \ldots, x_{i,D}(t)) \\ &\boldsymbol{v}_i(t) = (v_{i,1}(t), v_{i,2}(t), \ldots, v_{i,D}(t)) \\ &\boldsymbol{x}_i(t), \boldsymbol{v}_i(t) \in R^D \qquad i = 1, 2, \ldots, S \end{aligned} \tag{3}$$

where each dimension of a particle in the swarm is updated using the following equations:

$$\begin{aligned} v_{i,j}(t) &= w(t) v_{i,j}(t-1) \\ &\quad + c_1 r_1 [P_i(t-1) - x_{i,j}(t-1)] \\ &\quad + c_2 r_2 [P_g(t-1) - x_{i,j}(t-1)] \\ x_{i,j}(t) &= x_{i,j}(t-1) + v_{i,j}(t) \end{aligned} \tag{4}$$

In Eq. (4), c_1 and c_2 denote constant coefficients, and r_1 and r_2 are elements from random sequences in the range of (0, 1). The parameter c_1 controls the influence degree of cognitive part of an individual, and c_2 determines the effect of social part of the swarm. The inertia weight w is decreased linearly, starting from one point and ending at the other point related to maximum iteration number G. The personal best-position vector of each particle is computed using the following expression:

$$P_i(t) = \begin{cases} P_i(t-1) & \text{if } f(\boldsymbol{x}_i(t)) \ge f(P_i(t-1)) \\ \boldsymbol{x}_i(t) & \text{if } f(\boldsymbol{x}_i(t)) < f(P_i(t-1)) \end{cases} \tag{5}$$

Then the global best-position vector is found by

$$P_g(t) = \arg \min_{P_i(t)} f(P_i(t)) \tag{6}$$

The drawback of PSO is due to the lack of diversity. Therefore, we applied mutation operations during the generations. Mutation operators introduce new individuals into a population by manipulating of a current individual, thus adding diversity into the population and probably preventing stagnation of the search in local optima. The traditional general form of the mutation, which was applied in classical PSO algorithm, can be written as $x_{i,j}(t) = M(x_{i,j}(t))$, where M is the mutation operator providing the offspring vector. Instead of this strict form of a mutation operator, it can be described including mutation strategy as follows:

$$x_{i,j}(t) = F(M(x_{i,j}(t)), f_m) \tag{7}$$

where F is the generalized mutation function, f_m is a user-defined frequency. In every f_m^{-1} period of the generations applying the mutation operator to all particle dimensions of the whole swarm, individuals in the population spread throughout the design space. The mutation operator is given by

$$x_{i,j}(t) = x_{i,j}(t)[1 + A.\text{rand}.\delta], \quad \begin{matrix} j = 1, 2, \ldots, D \\ i = 1, 2, \ldots, S \end{matrix}$$
$$\delta = \begin{cases} 1 & \text{if } t = nf_m, n = 1, 2, \ldots \\ 0 & \text{if } t \neq nf_m \end{cases} \tag{8}$$

where A is a user-defined scale factor called an amplitude, which may be selected as a fixed number or computed during the iterations, and rand is a real random number specified by a random number generator.

The PSO parameters used in applications were selected based on a careful prior study [16]. Therefore, during the optimization processes, the swarm size S is taken as 10, the inertia weight w is decreased linearly, starting from 0.6 and ending at 0.3 related to maximum iteration number G, which is equal to 100. The mutation frequency f_m is equal to 5, scale factor A is equal to 0.5, c_1 is equal to 2, and c_2 is equal to 2. In the computational phase, two-level parallelization is implemented. The first parallelization is applied in the swarm. Each particle objective-function value within the swarm is computed on different processors in a parallel way. The flow solver code is also appropriate for parallel computing. Therefore, the second level parallelization is applied in the flow solver.

2. Gradient-Based Optimization Algorithm

In the present study, sequential quadratic programming (SQP) is used to solve the optimization problems. SQP is one of the most powerful methods among the mathematical nonlinear programming techniques. However, it has a major convergence disadvantage in distinguishing a local optimum point from a global one. Non-gradient-based methods, such as PSO, have the ability to escape from the local minimums. To escape from the local minimum, many initial points for all cases were used in this study. In this method, we first generate a quadratic approximation to the objective function using the Taylor series expansion of the objective function. The solution of the quadratic problem is used to determine the search direction at a given point. The quadratic problem is expressed as follows:

$$\begin{aligned} &\min \nabla f(\boldsymbol{x})^T \boldsymbol{s} + \tfrac{1}{2}\boldsymbol{s}^T H \boldsymbol{s} \\ &\text{subject to } \nabla g_j(\boldsymbol{x})^T \boldsymbol{s} + g_j(\boldsymbol{x}) \leq 0 \\ &\nabla h_k(\boldsymbol{x})^T \boldsymbol{s} + h_k(\boldsymbol{x}) = 0 \end{aligned} \tag{9}$$

The search direction vector $\boldsymbol{s}$ is the design variable for this quadratic problem. The matrix H is initially the identity matrix, which is a positive definite matrix. To approach the Hessian of the objective function, H is updated on the subsequent iterations [17]. The gradient-based optimization process may be summarized as follows:

For the initiation,
$i = 0, \boldsymbol{x} = \boldsymbol{x}^0$.
$i = i + 1$.
Calculate $f(\boldsymbol{x}^{i-1})$ and $g_j(\boldsymbol{x}^{i-1})$ for $j = 1, m$.
Identify the set of critical constraints J_c.
Evaluate $\nabla f(\boldsymbol{x}^{i-1})$ and $\nabla g_j(\boldsymbol{x}^{i-1})$ for $j \in J_c$.
Determine a search direction $\boldsymbol{s}$.
Investigate a one-dimensional search to find step size α.
Set $\boldsymbol{x}^i = \boldsymbol{x}^{i-1} + \alpha \boldsymbol{s}$.
Check for convergence; if not, go to second step.
Stop.

C. Design Parameters and Objective Function

A nonlinear-constrained optimization problem for an airfoil can be expressed as follows:

$$\begin{aligned} &\min f_{X \in R^D} = \frac{C_D}{C_L} \\ &\text{subject to } -C_L + C_L^* \leq 0 \\ &x^L \leq x \leq x^U \end{aligned} \tag{10}$$

where C_L^* is the design lift coefficient. In the PSO algorithm, the cost-function description can be converted into a unique equation by using a weighting number [18], such as

$$f_{x \in R^D} = \frac{C_D}{C_L} + 10(C_L^* - C_{L2})^2$$
$$C_{L2} = \begin{cases} C_L^* & \text{if } C_L \geq C_L^* \\ C_L & \text{if } C_L < C_L^* \end{cases} \tag{11}$$

In both optimization processes, the following design parameters are used: mass flow coefficient C_q, center location of actuator x_c, and suction/blowing angle relative to the local tangent, β. Depending on the number of actuators used in AFC, the design-parameter vector $\boldsymbol{x}$ is composed of different combinations based on given parameters. In the first three test cases, the center locations of the actuators are kept fixed, and the velocities and angles are selected as design variables. However, for the last three cases, the locations of the actuators are also selected as additional design variables. For all the cases, the width of the actuator is $0.035c$, as used in the experiment. The design variables and fixed locations for the first three cases are depicted in Fig. 1. The first location, $0.7075c$, is selected as the validation point. This location is used by Smith and Walker [7] in their experimental studies as the hinge line of the trailing-edge flap. The third location, $0.5125c$, is placed behind of the shock wave. Under selected flow conditions, the center of normal shock wave occurs about $0.5100c$. The second location, $0.61775c$, is placed between the first and the third locations.

D. Grid Generation

A two-dimensional, 10%-thick, symmetric NACA 64A010 is used as the test airfoil. Two different grid morphologies are used during the simulations. The first one (given in Fig. 2a) is the grid with clustering in the normal direction and in the vicinity of jets to resolve the details of the flow for the first three cases. The second grid (given in Fig. 2b) is used for the last three cases, and the travel area of the actuator locations between $0.5500c$ and $0.9600c$ is made dense. The resolution of the first-used C-type computational grid is 407×121 and the second one is 449×121. Normal spacing for the first grid line of the surface of the airfoil is $0.000001c$. Each grid is divided into four subblocks to implement the parallel computing for faster computation.

III. Validation and Grid Sensitivity

The NACA 64A010 airfoil was tested by Smith and Walker [7] at different transonic speeds with surface mass injection downstream of the hinge line of the trailing-edge flap. The validation cases used in this study had a Reynolds number of 2.9×10^6 based on airfoil chord, $M_\infty = 0.78$, and $\alpha = 0.5°$, corresponding to one of the wind-tunnel experiments. The region of suction was located between $0.69c$ and $0.725c$, which is downstream of the shock position without

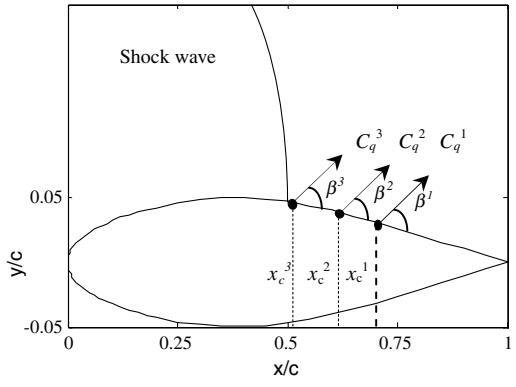

Fig. 1 Design parameters for active flow control.

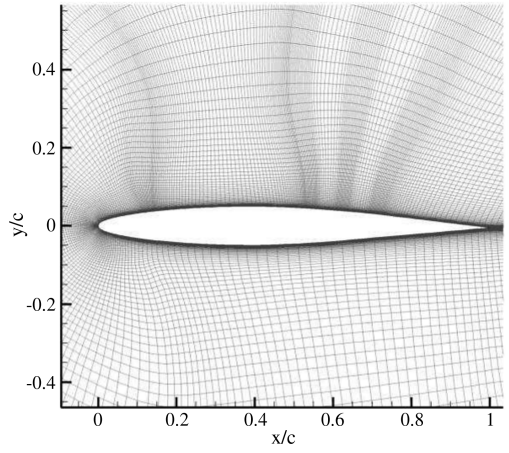

a)

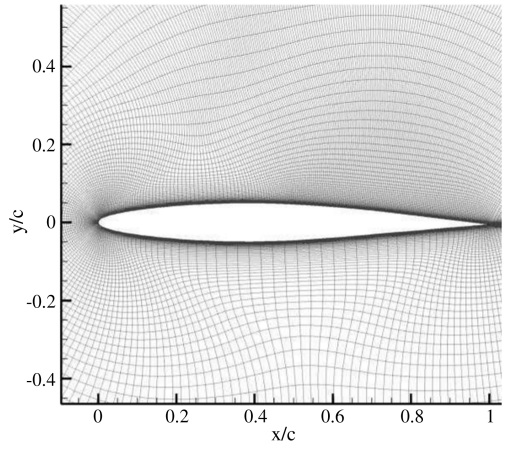

b)

Fig. 2 Computational grids used in simulations: a) for the first three cases and b) for the last three cases.

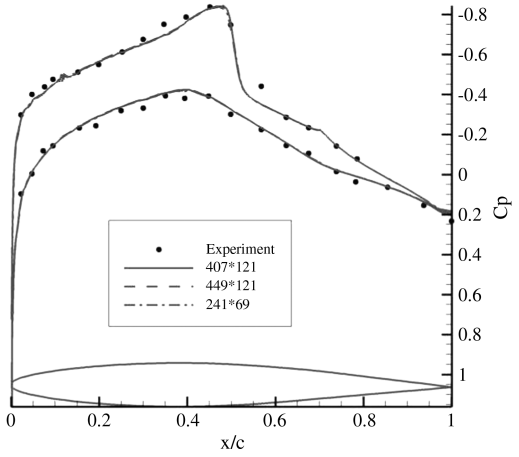

a) C_p distribution without AFC

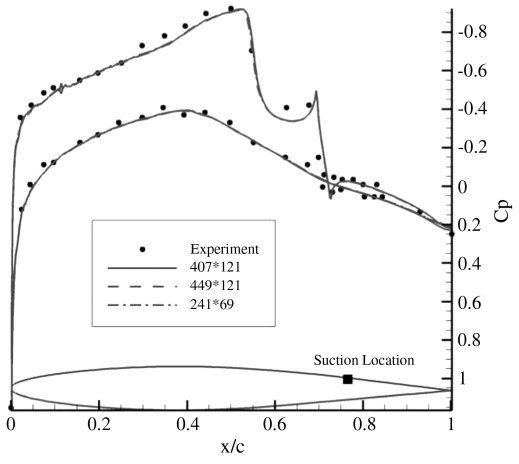

b) C_p distribution with AFC

Fig. 3 Comparison of pressure distributions for a NACA 64A010 airfoil.

active flow control. The suction coefficient was −0.06429 and the suction angle was 84° to the airfoil surface.

Shown in Fig. 3 is the comparison of the pressure distributions for both the computation and the experiment with and without flow control. Solution sensitivity to the grid used in this study is illustrated in Table 1. For the computational cases, three sets of grids and another computational result given by Qin et al. [19] have been used. Normalized first cell-height y^+ values, based on the height of the first wall-bounded cell, are below unity for all the meshes considered here. The solutions obtained on the course and fine grids are reasonably good. The results obtained on these three different grid sizes are reasonably converged results and show very little grid sensitivity. The results seem to be in qualitative agreement with the experimental data. Additionally, a thorough the discussion of the adequacy of this widely used and well-accepted flow solver can be found in [20,21]. As can be seen from Table 1, the measured lift for the control case and drag for the noncontrol values are different from the present results. The reason may be due to the fixtures mounted on the airfoil in the experiment, which was not calculated in the computation.

IV. Optimization Results

A. Fixed-Location Optimizations

The effects of mass flow coefficient and angle for different numbers of actuators at fixed locations are investigated. For that reason, three cases depending on the number of actuators are studied. First, only one actuator is considered. Then the number of actuators is increased to two, then to three, to control the flow on the airfoil's upper surface.

1. One-Actuator Optimization

The center of suction/blowing actuator is placed on $0.7075c$. The design-parameter vector and bounds are described as

$$\boldsymbol{x} = [C_q \beta]^T \qquad -0.1 \le C_q \le 0.025 \qquad 3^\circ \le \beta \le 176^\circ \quad (12)$$

Because of the global nature of the PSO algorithm and relatively small number of design parameters, the optimization process takes only two generations. At the end of optimization, C_q has taken the maximum suction velocity as −0.1, and β became the minimum angle of 3°, which is almost parallel to the local airfoil surface. The changes in aerodynamic coefficients C_L and C_D versus CFD calls

Table 1 Grid sensitivity for NACA 64A010 airfoil test cases

Grid size	C_L	C_D
Without control		
449 × 121	0.2121	0.01050
407 × 121	0.2111	0.01059
241 × 69	0.2121	0.01071
Experiment [7]	0.2000	0.01300
Computation [19]	0.2166	0.01110
449 × 121	0.2821	0.01406
407 × 121	0.2773	0.01376
With control		
241 × 69	0.2751	0.01378
Experiment [7]	0.2400	0.01400
Computation [19]	0.2795	0.01380

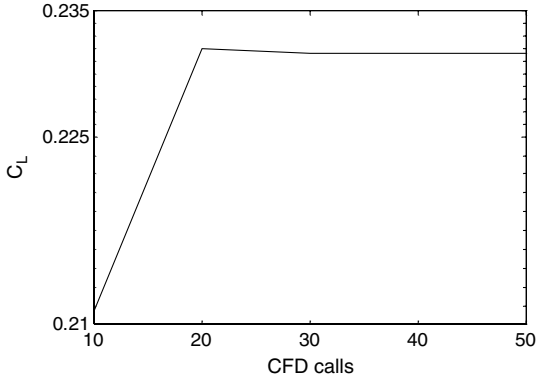

a) Convergence history for C_L

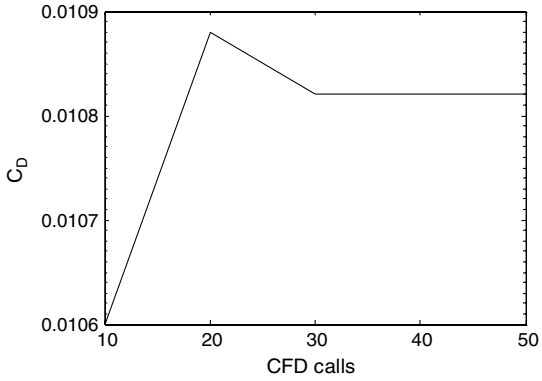

b) Convergence history for C_D

Fig. 4 Change of aerodynamic coefficients during the generations.

belonging to the best particle are depicted in Fig. 4. According to these figures, both coefficients are increased due to the suction control. However, the aerodynamic performance based on L/D is also increased. The reason is that the increment in C_L is larger than the increment in C_D. After suction operation at optimal values, C_L is increased 9.76%; on the other hand, C_D is increased 2.17%. As a result, the redescribed objective-function value $(1/f)$ is increased 7.43%.

The change in aerodynamic performance versus CFD calls in PSO is shown in Fig. 5a. Figure 5b depicts the same objective-function change versus CFD calls in the SQP optimization process. In this gradient-based optimization process, six different initial points (i.p.) are tested to avoid local optimums. After these six SQP optimization processes, the same optimal values found in the PSO process are determined. The PSO case needs 20 CFD calls to reach the optimal values. However, SQP needs a total of 66 CFD calls based on six different initial points to get the same optimal values. Although sequential computations are implemented, only the best SQP process and the PSO process are compared in terms of computation time in Fig. 5c. One CFD call takes approximately 24 min based on an Intel 2.4 GHz quad-core processor. According to this figure, the PSO approach is much more time-efficient than the SQP approach.

2. Two-Actuator Optimization

The centers of suction/blowing actuators are placed on $0.7075c$ and $0.61775c$ points. The design-parameter vector and bounds are described as follows:

$$\begin{aligned} \boldsymbol{x} &= [C_q^1 \beta^1 C_q^2 \beta^2]^T \\ -0.1 &\le C_q^i \le 0.025 \\ 3^\circ &\le \beta^i \le 176^\circ |^{i=1,2} \end{aligned} \tag{13}$$

PSO optimization process takes only four generations. At the end of the optimization, $C_q^{1,2}$ have taken the maximum suction velocity as

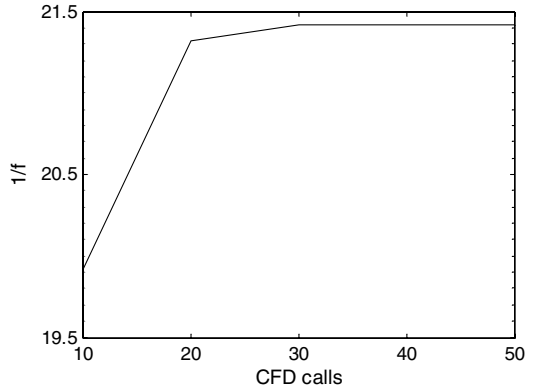

a) Objective function change versus CFD calls in PSO run

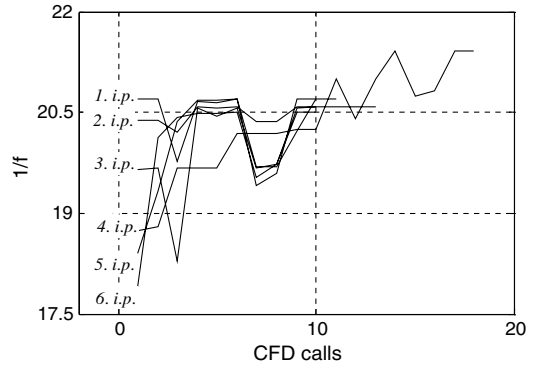

b) Objective function change versus CFD calls in SQP runs

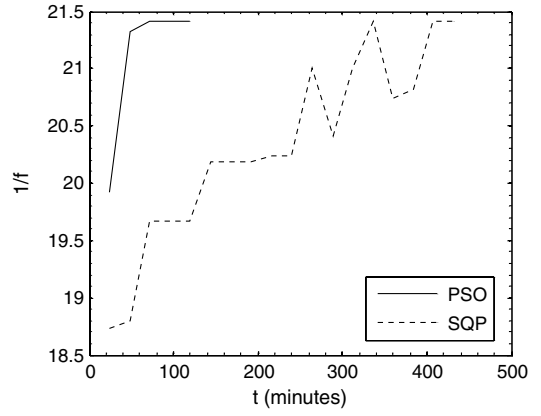

c) Comparison between SQP and PSO

Fig. 5 Change of aerodynamic performance in PSO and SQP.

-0.1, and $\beta^{1,2}$ became the minimum angle of 3°. The changes of aerodynamic coefficients C_L and C_D versus CFD calls belonging to the best particle are depicted in Fig. 6. Similar to the previous operation, both coefficients are increased due to suction operations. After suction operations at optimal values, C_L is increased 16.86%; on the other hand, C_D is increased 3.21%. As a result, $1/f$ is increased 13.25%.

The change in aerodynamic performance versus CFD calls in PSO is shown in Fig. 7a. Figure 7b depicts the same objective-function change versus CFD calls in the SQP optimization process. A total of five different initial points are tested to escape from local optimums. After these five SQP optimization processes, the same optimal values found in the PSO process are determined. In the PSO process, 40 CFD calls are needed to reach the optimal values. However, with SQP, 48 CFD calls are needed to get the same optimal values. Although sequential computations are implemented, only the best SQP process and PSO process are compared in terms of computation time in Fig. 7c. Similar to the previous optimization case, the PSO approach is much more time-efficient than the SQP approach.

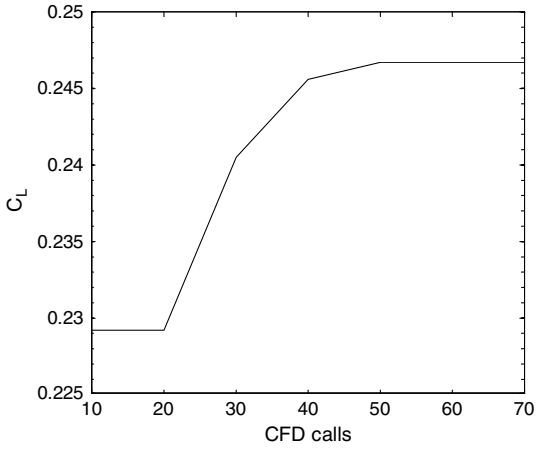

a) Convergence history for C_L

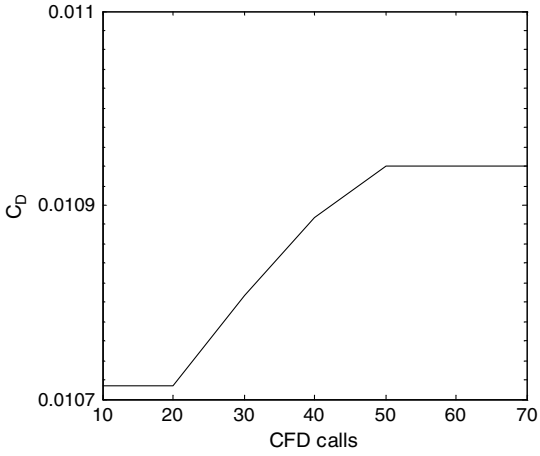

b) Convergence history for C_D

Fig. 6 Change of aerodynamic coefficients during the generations.

3. Three-Actuator Optimization

The centers of suction/blowing actuators are placed on $0.7075c$, $0.61775c$, and $0.5125c$ points. The design-parameter vector and bounds are described as follows:

$$\boldsymbol{x} = [C_q^1 \beta^1 C_q^2 \beta^2 C_q^3 \beta^3]^T$$
$$-0.1 \le C_q^i \le 0.025$$
$$3^\circ \le \beta^i \le 176^\circ |^{i=1,2,3} \tag{14}$$

PSO optimization process takes 11 generations. At the end of the optimization, $C_q^{1,2,3}$ has taken the suction velocity as -0.0864, -0.1, and -0.0977, respectively, and $\beta^{1,2,3}$ became the minimum angle of 3°. The changes of aerodynamic coefficients C_L and C_D versus CFD calls belonging to the best particle are depicted in Fig. 8. After suction operations at optimal values, C_L is increased 22.03%; on the other hand, C_D is increased 4.82%. As a result, $1/f$ is increased 16.46%. The change in aerodynamic performance versus CFD calls in PSO is shown in Fig. 9a. Figure 9b depicts the same objective-function change versus CFD calls in the SQP optimization process. In total, four different initial points are tested to escape from local optimums based on previous experience. After these four SQP optimization processes, slightly different optimal values are determined. With SQP, all C_q variables are determined as -0.1 suction velocity; however, all angle values are the same as they are in with the PSO. In SQP, the aerodynamic performance is 16.26%, which is slightly smaller than it is in PSO. In total, 110 CFD calls are needed to reach the optimal values with PSO. However, SQP needs 65 CFD calls to get the same optimal values. The best SQP process

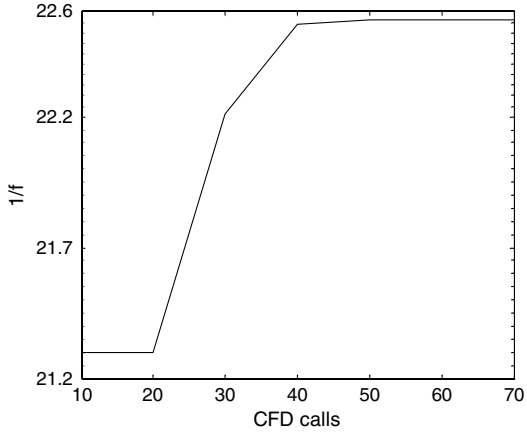

a) The objective function change versus CFD calls in PSO run

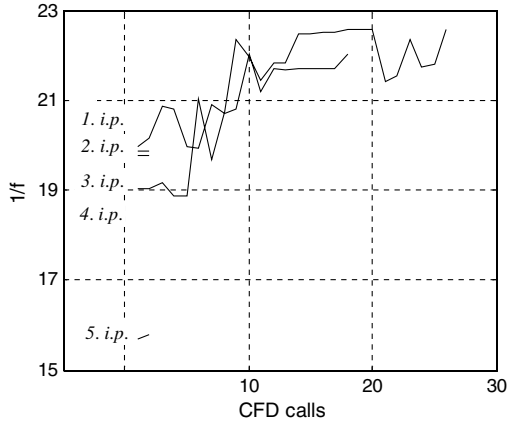

b) The objective function change versus CFD calls in SQP runs

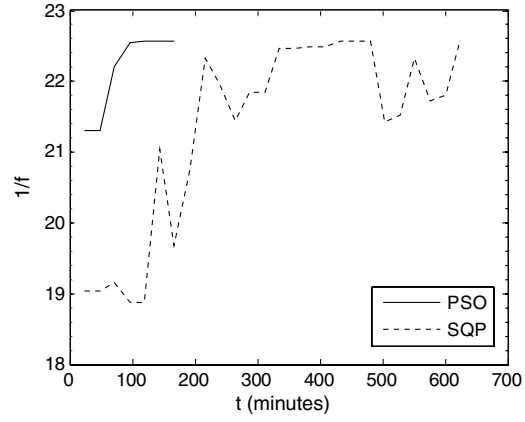

c) Comparison between SQP and PSO

Fig. 7 Change of aerodynamic performances in PSO and SQP processes.

and PSO process are compared in terms of computation time on the right side of Fig. 9c. Although SQP is more efficient than PSO process in terms of CFD calls, the PSO approach is more time-efficient than the SQP approach.

B. Variable-Location Optimizations

The effects of mass flow coefficient, blowing/suction angle, and location of the center of the actuator for different numbers of actuators are investigated. Similar to previous case studies, three cases depending on the number of actuators are studied. First, only one actuator is considered. Then the number of actuators is increased to two then three actuators to control the flow on the airfoil upper surface.

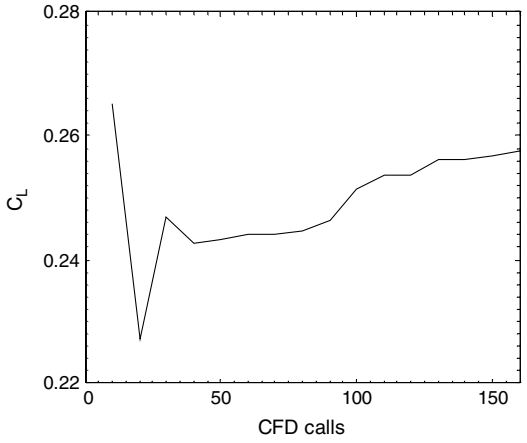

a) Convergence history for C_L

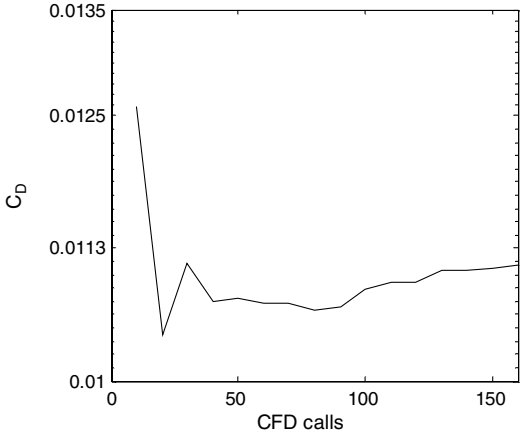

b) Convergence history for C_D

Fig. 8 Change of aerodynamic coefficients during the generations.

1. One-Actuator Optimization

The design-parameter vector and bounds are described as follows:

$$\begin{aligned} &\boldsymbol{x} = [C_q \beta x_c]^T \\ &-0.1 \le C_q \le 0.025 \\ &3^\circ \le \beta \le 176^\circ \\ &0.55c \le x_c \le 0.96c \end{aligned} \tag{15}$$

The PSO optimization process takes only four generations. At the end of optimization, C_q has taken the maximum suction velocity as -0.1, β became the minimum angle of 3°, and the location arrived at $0.5561c$, which is close to shock wave. These are the same as in the fixed-location case, except the location. However, the remaining result is different. The changes of aerodynamic coefficients C_L and C_D and the aerodynamic performance $1/f$ versus CFD calls belonging to the best particle are depicted in Fig. 10. After suction operation at optimal values and optimal location, C_L is increased 8.02%; on the other hand, C_D is decreased 1.33%. As a result, $1/f$ is increased 9.46%. This result is reasonably better than the fixed-location optimization case for one actuator. Another noteworthy point is that the drag is decreased due to the change in the location.

2. Two-Actuator Optimization

The design-parameter vector and bounds are described as follows:

$$\begin{aligned} &\boldsymbol{x} = [C_q^1 \beta^1 x_c^1 C_q^2 \beta^2 x_c^2]^T \qquad -0.1 \le C_q^i \le 0.025 \\ &3^\circ \le \beta^i \le 176^\circ|^{i=1,2} \qquad 0.70c \le x_c^1 \le 0.90c \\ &\qquad 0.55c \le x_c^2 \le 0.65c \end{aligned} \tag{16}$$

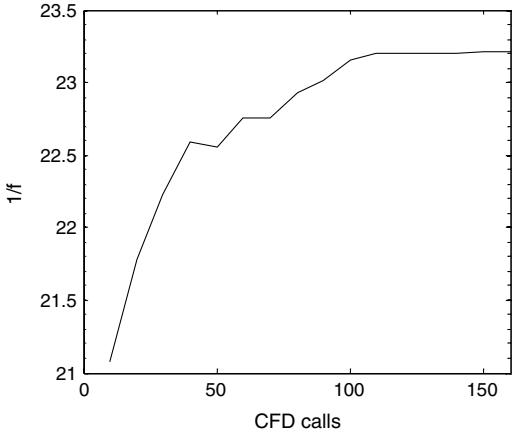

a) The objective function change versus CFD calls in PSO run

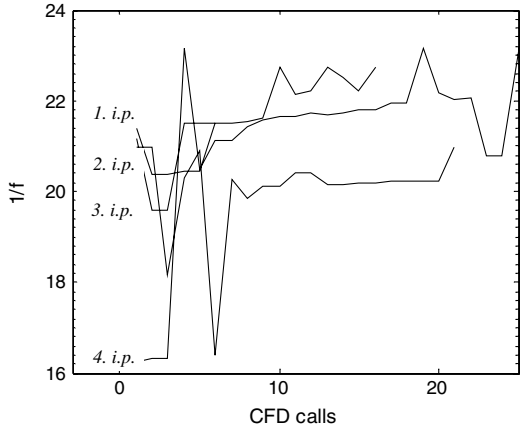

b) The objective function change versus CFD calls in SQP runs

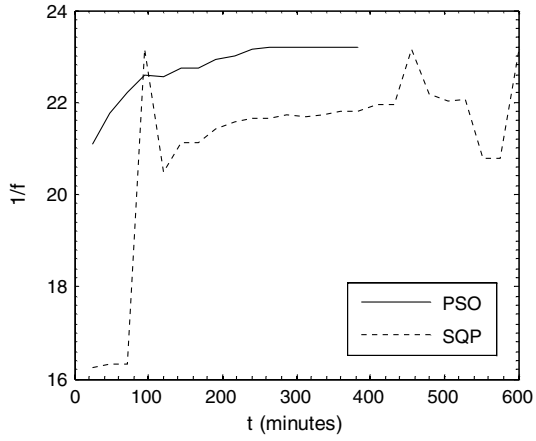

c) Comparison between SQP and PSO

Fig. 9 Change of aerodynamic performance in PSO and SQP processes.

To avoid the geometrical interaction, a $0.05c$ distance is kept between the actuators. The PSO optimization process takes six generations. At the end of optimization, both C_q variables have taken the maximum suction velocity as -0.1; similarly, both β angles became the minimum angle of 3°; and the first location x_c^1 is arrived at $0.5724c$, which is close to the shock wave and the second location is x_c^2 arrived at $0.7000c$. These are the same values as in the fixed-location case, except the locations. The changes of aerodynamic coefficients C_L and C_D and performance $1/f$ versus CFD calls belonging to the best particle are depicted in Fig. 11. After suction operations at optimal values and optimal locations C_L is increased 17.68%; on the other hand, C_D is increased 1.71%. As a result, $1/f$ is

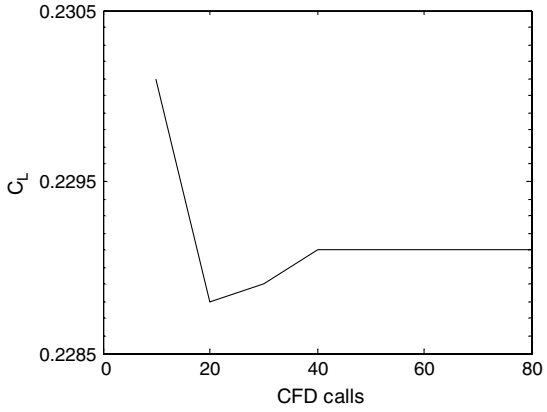

a) C_L versus CFD calls

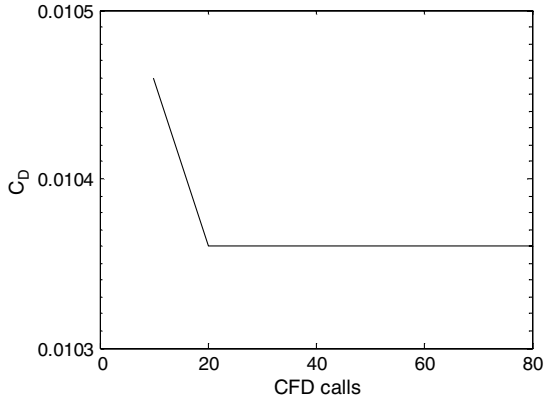

b) C_D versus CFD calls

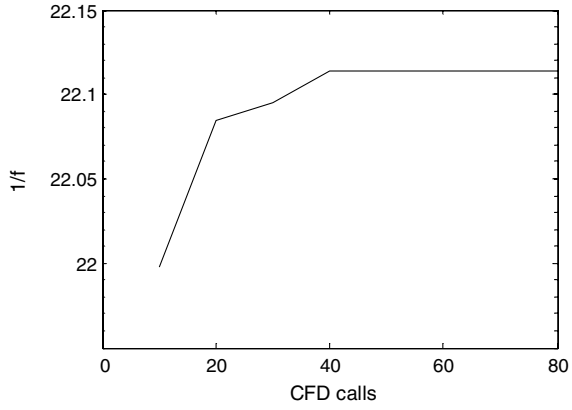

c) Objective function versus CFD calls

Fig. 10 Change of aerodynamic coefficients and performance during the generations.

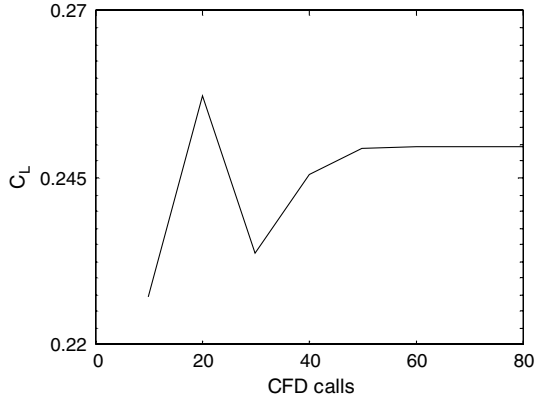

a) C_L versus CFD calls

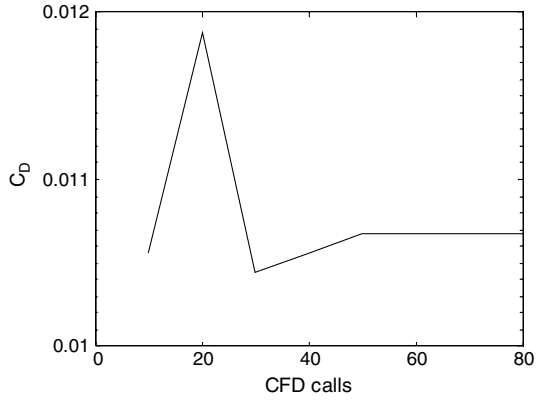

b) C_D versus CFD calls

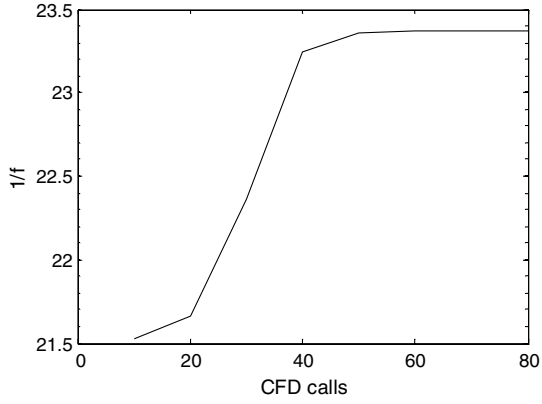

c) Objective function versus CFD calls

Fig. 11 Change of aerodynamic coefficients and performance during the generations.

increased 15.69%. This result is much better than the fixed-location optimization case for two actuators.

3. Three-Actuator Optimization

The design-parameter vector and bounds are described as follows:

$$\boldsymbol{x} = [C_q^1 \beta^1 x_c^1 C_q^2 \beta^2 x_c^2 C_q^3 \beta^3 x_c^3]^T \qquad -0.1 \le C_q^i \le 0.025$$
$$3^\circ \le \beta^i \le 176^\circ|^{i=1,2,3} \qquad 0.85c \le x_c^1 \le 0.96c$$
$$0.70c \le x_c^2 \le 0.80c \qquad 0.55c \le x_c^3 \le 0.65c \tag{17}$$

Similar to the previous case study, to avoid the geometrical interaction among the actuators, a $0.05c$ distance is kept between the actuators. The PSO optimization case needs 11 generations. At the end of optimization, $C_q^{1,2,3}$ have taken the suction velocity as -0.1, -0.077, and -0.1, respectively; $\beta^{1,2,3}$ became the minimum angle of 3°; the first location x_c^1 is arrived at $0.5889c$, which is close to the shock wave; the second location x_c^2 is arrived at $0.7700c$; and the third location x_c^3 is arrived at $0.9600c$. The changes of aerodynamic coefficients C_L and C_D and the performance $1/f$ versus CFD calls belonging to the best particle are depicted in Fig. 12. After suction operations at optimal values and optimal locations, C_L is increased 37.48%; on the other hand, C_D is increased 14.29%. As a result, $1/f$ is increased 20.7%. This result is much better than the fixed-location optimization case for three actuators.

C. Comparative Evaluations

Both studies showed that the number of actuators and their locations have important effects on the aerodynamic performance. In Fig. 13, the relationship between the number of actuators and performance is depicted. Using more actuators on the airfoil surface

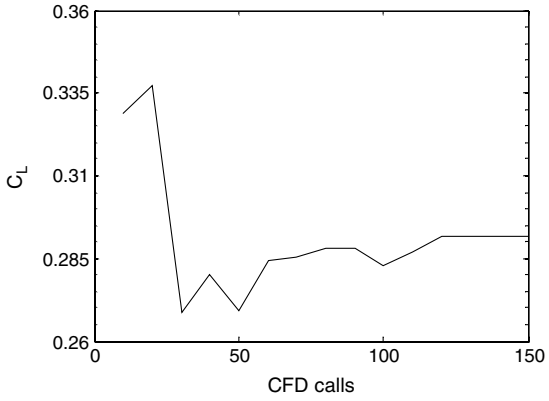

a) C_L versus CFD calls

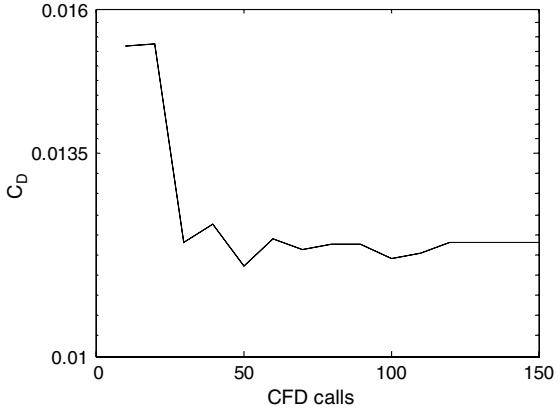

b) C_D versus CFD calls

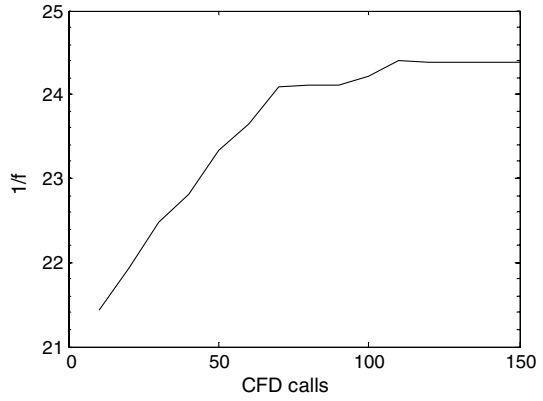

c) Objective function versus CFD calls

Fig. 12 Change of aerodynamic coefficients and performance during the generations.

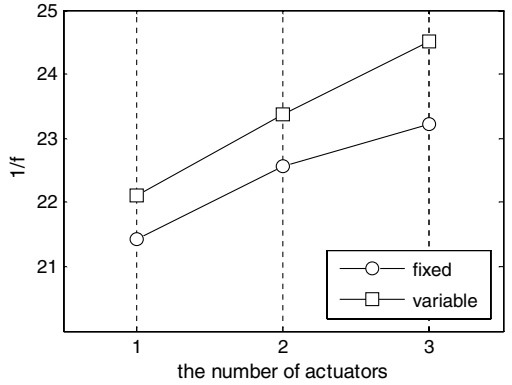

Fig. 13 Effect of location and the number of actuators on an aerodynamic performance.

provides more increase in the aerodynamic performance. The increasing trend looks like an exponential curve. Selection of actuator location is the other emphasized point. Instead of determining the locations based on rudimentary guessing, using optimized locations provides more efficient results. As can be seen in Fig. 13, using only two actuators at proper locations can provide almost the same level aerodynamic performance increase as using three actuators.

On the other hand, using an actuator causes the change in the location of the shock wave. In all the cases, the shock location moves downstream. In Fig. 14a, the pressure contours are shown for a fixed-location case using one actuator. Because of suction at $0.7075c$ point, a local pocket is generated. This pocket pushes the shock to $0.5625c$, which is farther than the original location of $0.5100c$. In Fig. 14c, the pressure contours are shown for the optimized-location case with one actuator. Similar to the fixed-location case, because of the suction at

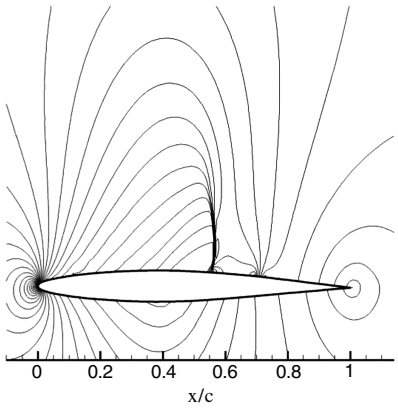

a) The pressure contours for a fixed-location case using one actuator

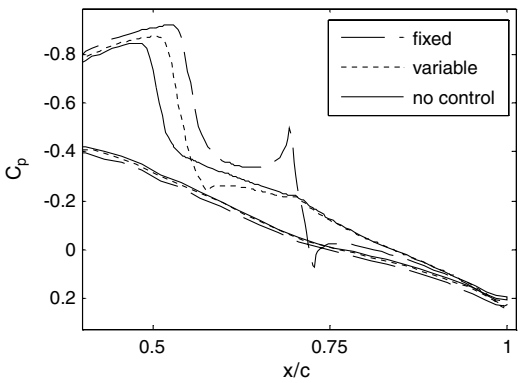

b) The effects of both suction operations on the pressure coefficient distributions

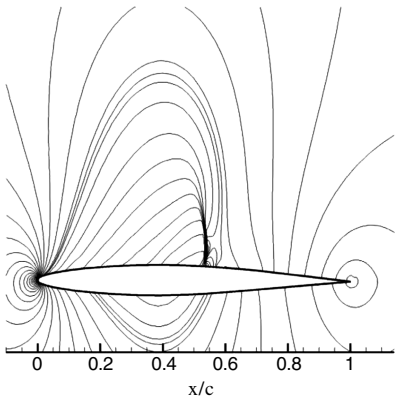

c) The pressure contours for the optimized location case

Fig. 14 Effect of control on the pressure field and coefficient for the one-actuator case.

the 0.5561c point, a local pocket is generated. This pocket pushes the shock to 0.5350c. The effects of both suction operations on the pressure coefficient can be seen in Fig. 14b. Selecting a fixed location causes a sharp increase and then a sharp decrease in the C_p distribution. However, suction at the optimal location causes a relatively small and smooth decrease and then a remarkable increase in the C_p distribution. In both cases, it is observed that the shock is pushed downstream as compared to the no-suction cases.

In Fig. 15a, the pressure contours are shown for the fixed-location case with two actuators. Because of suction at the 0.7075c and 0.61775c points, two separate pockets are generated. As a consequence, the shock wave is located at 0.5400c. The resulting effect on the pressure coefficient distribution can be seen in Fig. 15b: sharp increases and decreases are visible. In Fig. 15c, the pressure contours are shown for the optimized locations of the two actuators. Because of suction at the 0.5724c and 0.7000c points, only a single local pocket is generated and the shock is pushed further aft to 0.5500c. The resulting effect on the pressure coefficient distribution is a relatively smooth decrease followed by an increase. Again, in both cases, it is observed that the shock is pushed downstream as compared to the no-suction cases.

In Fig. 16a, the pressure contours are shown for the fixed-location case with three actuators. Because of suction at the 0.7075c, 0.61775c, and 0.5125c points, now three pockets are generated. As a consequence, the shock wave is located at 0.5525c. In Fig. 16c, the pressure contours are shown for the optimized locations. Suction at the 0.9600c, 0.7700c, and 0.5889c points generate a merged pocket and an additional single pocket. Consequently, the shock wave is

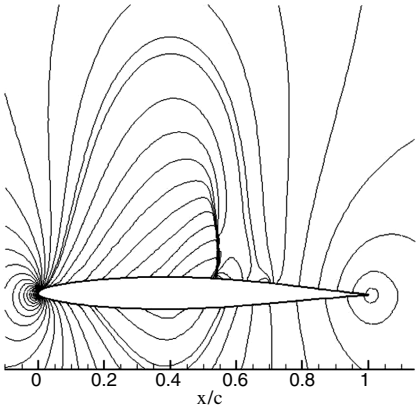

a) The pressure contours for the fixed-location case with two actuators

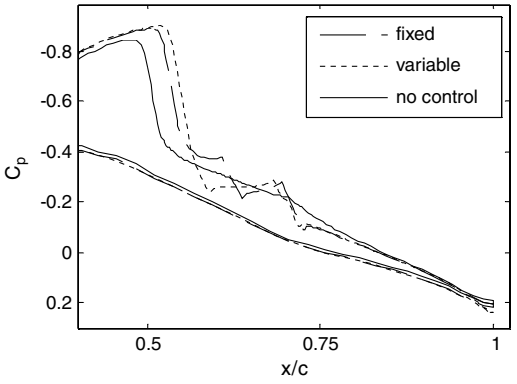

b) Resulting effects on the pressure coefficient distributions

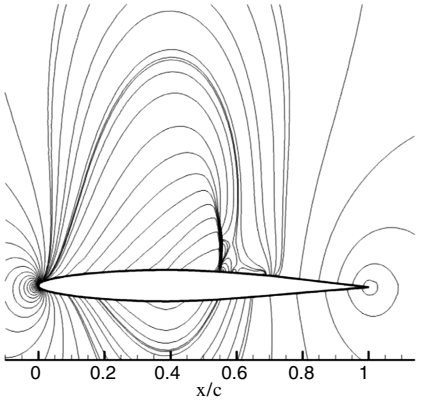

c) The pressure contours for the optimized locations of the two actuators

Fig. 15 Effect of location on pressure field and coefficient for the two-actuator case.

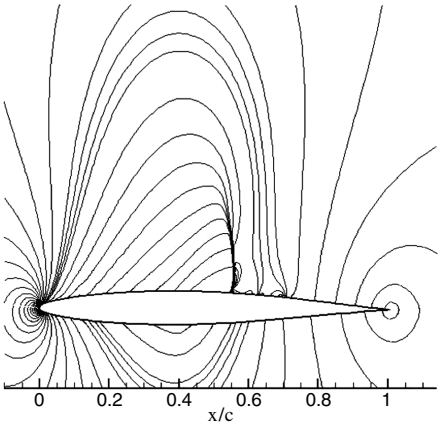

a) The pressure contours for the fixed-location case with three actuators

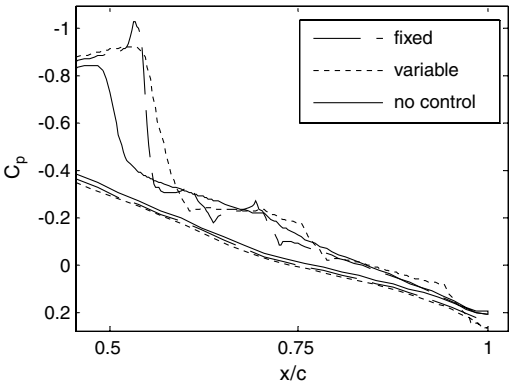

b) Resulting effects on the pressure coefficient distributions

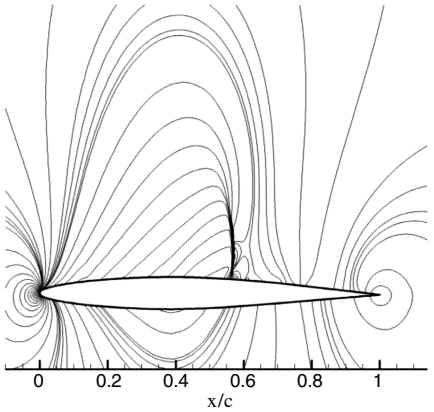

c) The pressure contours for the optimized locations

Fig. 16 Effect of location on pressure field and coefficient for the three-actuator case.

pushed aft to $0.5650c$, which is the farthest downstream point of all the cases. The effect of the fixed-location and the optimized-location suctions on the pressure coefficient distributions can be seen in Fig. 16b. Similar to previous cases, fixed-location cases cause sharp increases and decreases. However, suction at the optimal locations causes relatively smooth decrease and increase. Once again, in both cases, it is observed that the shock is pushed downstream, as compared to the no-suction cases.

In all the cases, pushing the shock more aft toward the trailing edge extends the supersonic region and shortens the subsonic area. Additionally, the optimization results in squeezing the suction locations to be closer or merged for improved aerodynamic performance.

V. Conclusions

In the first part of the present paper, computational simulations are reported to investigate the benefits of AFC in improving the aerodynamic performance of a 2-D airfoil at a transonic speed and by using the heuristics-based optimization technique PSO and the gradient-based optimization technique SQP. The suction and blowing angles and mass flow coefficients are taken as the design variables in the studied one-actuator, two-actuator, and three-actuator cases. A Navier–Stokes solver is coupled with both optimizers to obtain the necessary flow analyses for the initial design parameters and to then improve the aerodynamics of the airfoil via the optimization.

As a gradient-based optimization method's success depends heavily on the initial design point, several optimization runs with different initial values are needed to avoid the local minima. Therefore, it is generally observed that PSO approach is more efficient than the SQP in terms of time and CFD calls.

Using more actuators provides better aerodynamic performance. However, this trend is exponential. Suction operations result in increases in both lift and the drag for all the cases. But C_L increase is more than that of C_D, resulting in better aerodynamic performance. The best result is provided by the three-actuator case with a 16.46% increase in the aerodynamic performance. Additionally, the shock wave location on the upper surface is moved toward the trailing edge, resulting in the extension of the supersonic region for all the cases.

In the second part of the present paper, computational cases are reported to investigate the benefits of AFC on the aerodynamic performance of the same airfoil under the same flow conditions by using PSO. The suction and blowing angles, mass flow coefficients, and the locations of the actuators are taken as the design variables in the one-actuator, two-actuator, and three-actuator cases. A Navier–Stokes solver is coupled with the PSO optimizer to obtain a flow solution for a given initial design and to then improve the aerodynamics of the airfoil via the optimization.

Similar to the previous cases, using more actuators provides better aerodynamic performance. Suction operations result in increased C_L and either decreased or increased C_D. The one-actuator case provides a particularly interesting result, because C_D is decreased and C_L is increased in this case. The best result is provided by the three-actuator case, with a 20.7% increase in the aerodynamic performance. All of the cases provide better results than their fixed-location counterparts. Again, the shock wave location on the upper surface is further aft toward the trailing edge, resulting in the extension of the supersonic region for all the cases. Another noteworthy point is that the optimization processes move closer or merge with the actuator locations, which effectively provides a more global suction.

Finally, it is concluded that AFC can provide high aerodynamic performance enhancement by optimizing its parameters. However, AFC alone may not be sufficient to get the best designs. Therefore, it is recommended as a follow-up to study simultaneous AFC and passive flow control techniques.

References

[1] Gad-el-Hak, M., "Flow Control: The Future," *Journal of Aircraft*, Vol. 38, No. 3, May–June 2001, pp. 402–418. doi:10.2514/2.2796

[2] Kibens, V., and Bower, W. W., "An Overview of Active Flow Control Applications at the Boeing Company," 2nd AIAA Flow Control Conference, AIAA Paper 2004-2624, Portland, OR, July 2004.

[3] Chang, T. L., Zhang, J., and Tsai, H. M., "A Novel Method of Flow injection and Suction for Lift Enhancement," 46rd AIAA Aerospace Sciences Meeting and Exhibit, AIAA Paper 2008-335, Reno, NV, Jan. 2008.

[4] Duvigneau, R., and Visonneau, M., "Simulation and Optimization of Aerodynamic Stall Control Using a Synthetic Jet," 2nd AIAA Flow Control Conference, AIAA Paper 2004-2315, Portland, OR, July 2004.

[5] Huang, L., Huang, G., and LeBeau, R., "Optimization of Airfoil Flow Control Using a Genetic Algorithm with Diversity Control," *Journal of Aircraft*, Vol. 44, No. 4, 2007, pp. 1337–1349. doi:10.2514/1.27020

[6] Vadillo, J., Agarwal, R. K., and Hassan, A. A., "Active Control of Shock/Boundary Layer Interaction in Transonic Flow over Airfoils," 43rd AIAA Aerospace Sciences Meeting and Exhibit, AIAA Paper 2005-486, Reno, NV, Jan. 2005.

[7] Smith, D. W., and Walker, J. H., "Test of an Area Suction Flap on a NACA 64A010 Airfoil at High Subsonic Speeds," NASA TN D 310, 1960.

[8] Qin, N., Zhu, Y., and Shaw, S. T., "Numerical Study of Active Shock Control for Transonic Aerodynamics," *International Journal of Numerical Methods for Heat and Fluid Flow*, Vol. 14, No. 4, 2004, pp. 444–466. doi:10.1108/09615530410532240

[9] Qin, N., Zhu, Y., Ashill, P., and Shaw, S. T., "Active Flow Control of Transonic Aerodynamics Using Suction, Blowing. Bumps and Synthetic Jets," AIAA Paper 2000-4329, 2000.

[10] Vadillo, J., and Agarwal, R. K., "Numerical Study of Transonic Drag Reduction for Flow Past Airfoils Using Active Flow Control," AIAA Paper 2007-712, 2007.

[11] Meunier, M., "Simulations of Flow Control Strategies for Novel High-Lift Configurations," *AIAA Journal*, Vol. 47, No. 5, 2009, pp. 1145–1157. doi:10.2514/1.38245

[12] Yagiz, B., and Kandil, O., "Optimization of Active Flow Control in Transonic Aerodynamics," 27th AIAA Applied Aerodynamics Conference, AIAA Paper 2009-3763, San Antonio, TX, 22–25 June 2009.

[13] Krist, S. L., Biedron, R. T., and Rumsey, C. L., "CFL3D User's Manual Version 5.0," NASA TM-1998208444, June 1998.

[14] Liou, W. W., Huang, G., and Shih, T-H., "Turbulence Model Assessment for Shock Wave/Turbulent Boundary-Layer Interaction in Transonic and Supersonic Flows," *Computers and Fluids*, Vol. 29, 2000, pp. 275–299. doi:10.1016/S0045-7930(99)00010-9

[15] Eberhart, R. C., and Kennedy, J., "A New Optimizer Using Particle Swarm Theory," *Proceedings of the 6th International Symposium on Micromachine Human Science*, Nagoya, Japan, 1995, pp. 39–43.

[16] Pehlivanoglu, Y. V., "Hybrid Intelligent Optimization Methods for Engineering Problems," Ph.D. Dissertation, Aerospace Engineering Dept., Old Dominion Univ., Norfolk, VA, 2010.

[17] *VisualDOC User Manual*, Vanderplaats Research & Development, Inc., Colorado Springs, CO, 2002.

[18] Hacioglu, A., and Ozkol, I., "Vibrational Genetic Algorithm as a New Concept in Aerodynamic Design," *Aircraft Engineering and Aerospace Technology*, Vol. 74, No. 3, 2002, pp. 228–236.

[19] Qin, N., Zhu, Y., and Poll, D. I. A., "Surface Suction on Aerofoil Aerodynamic Characteristics at the Transonic Speeds," *Proceedings of the Institution of Mechanical Engineers, Part G (Journal of Aerospace Engineering)*, Vol. 212, 1998, pp. 339–351. doi:10.1243/0954410981532324

[20] Rumsey, C. L., "Case 3: RANS and URANS Application with CFL3D," http://ntrs.nasa.gov/archive/nasa/casi.ntrs.nasa.gov/20070031076_2007031972.pdf [retrieved 27 Sept. 2010].

[21] Hassan, A. A., "A Two-Point Active Flow Control Strategy for Improved Airfoil Stall/Post Stall Aerodynamics," 44th AIAA Aerospace Sciences Meeting and Exhibit, AIAA Paper 2006-99, Reno, NV, Jan. 2006.